Hollow-Shell Structured Porous $CoSe_2$ Microspheres Encapsulated by MXene Nanosheets for Advanced Lithium Storage

Lin Hong, [1,2] Shunlong Ju, [2] Yunhe Yang,[1] Jiening Zheng,[2] Guanglin Xia,[1] Zhenguo Huang,[3] Xiaoyun Liu*[1] and Xuebin Yu[2]*

[1] Key Laboratory of Specially Functional Polymeric Materials and Related Technology, Ministry of Education, School of Materials Science and Engineering, East China University of Science and Technology, Shanghai 200237, China

[2] Department of Materials Science, Fudan University, Shanghai 200433, China

[3] School of Civil & Environmental Engineering, University of Technology Sydney, Ultimo, New South Wales 2007, Australia

E-mail: yuxuebin@fudan.edu.cn; liuxiaoyun@ecust.edu.cn

Abstract: Cobalt diselenide ($CoSe_2$), a representative of transition-metal chalcogenides (TMCs), is attracting intensive interest for anode materials of lithium ion batteries (LIBs), in view of its high specific capacity based on conversion reaction mechanism. However, the huge volume variation and low intrinsic electrical conductivity during charge/discharge process lead to inferior rate performance and short cycle life of the $CoSe_2$ electrode, which severely hinder its practical application. Herein, novel hollow-shell structured porous $CoSe_2$ microspheres are constructed by selenization of Co-MOF based on the Kirkendall effect. Furthermore, $CoSe_2$@MXene robust structures, comprised of inner hollow $CoSe_2$ microspheres and outer MXene flakes coating, are fabricated by a facile electrostatic self-assembly method. The as-obtained $CoSe_2$@MXene hybrids possess combined advantages of high capacity of $CoSe_2$ hollow spheres and high conductivity of MXene flakes. More importantly, strong chemical

interactions (Co-O-Ti covalent bonds) between $CoSe_2$ and oxygen functionalized Ti_3C_2 MXene are formed at the interface, which could boost the electrons/ions transport kinetics and enhance the structural durability of $CoSe_2$@MXene hybrids, resulting in the improvement of rate performance and cycle stability. Consequently, as anode materials for LIBs, the $CoSe_2$@MXene hybrids deliver an admirable reversible capacity of 1051 mAh g^{-1} at 200 mA g^{-1}, a superior rate capability of 465 mAh g^{-1} at 5 A g^{-1}, and an excellent long-term cycle property at 1 A g^{-1} with a capacity of 1279 mAh g^{-1} after 1000 cycles. The hollow-shell structured porous materials coated by MXene strategy provides an effective route for designing new anode materials with excellent electrochemical properties.

Keywords: $CoSe_2$ hollow spheres, MXene, Co-O-Ti bond, Li-ion batteries

1. Introduction

With the increased demand for portable electronic devices and electric vehicles, the development of next-generation, high-energy, and high-power rechargeable lithium ion batteries (LIBs) has been attracting great attention.[1-5] However, commercial graphite, the current anode material with a low theoretical capacity (372 mA h g^{-1})[6], is far from meeting the demands of high-energy LIBs. In this regard, current scientific concern is focused on the development of advanced anode materials with high performance, environmentally friendly, and low cost, to break the barriers presented by graphitic carbon.

Among various alternatives, transition-metal chalcogenides (TMCs) have gained ever-growing interest in view of their relatively large lithium-storage capacity based on conversion reaction mechanism.[3, 5, 7-11] In particular, cobalt diselenide ($CoSe_2$), presents several other superiorities, such as intrinsically enhanced safety and wide availability except for the high specific capacity.[12-23] However, similar to other TMCs[24-26], $CoSe_2$ also suffers from huge volume variation upon the

charge/discharge processes, resulting in rapid capacity fading, and low intrinsic electrical conductivity, which usually causes inferior rate capability. Therefore, the rational design of structure and composition should be proposed to improve the electrochemical performance of TMCs.

One possible solution to address the limitation of huge volume variation is to design hollow structural nanomaterials with inner voids and functional shells. In such nanostructures, the stress-induced structural change of TMCs can be well alleviated during lithiation/delithiation processes, boosting their performance by providing enough space to accommodate the volume expansion. For example, Hu et al. reported the synthesis of hollow CoSe@carbon nanoboxes by a template reaction between zeolitic imidazolate framework 67 (ZIF-67) and Se powder, which exhibited excellent lithium-storage performance.[25] In addition, Liu et al. synthesized hollow SnS_2@CNTs carbon nanotubes, hollow SnS_2@CNBs carbon nanoboxes, and hollow SnS_2@CNSs carbon nanospheres by templating method, and these materials presented improved sodium storage performance due to their unique structural merits.[27]

In order to enhance the electrical conductivity of TMCs, a common strategy is to couple these compounds with conductive carbon-based materials, such as graphene[24], carbon nanotubes[28], functionalized carbon nanosheets[29], polydopamine[30], and glucose[5], to facilitate pathway for charge transport between selenide particles. However, the interface interaction between carbon-based matrix and active species is generally weak and the crystallinity of carbon materials is inferior, which hinder the transport of lithium ions and electrons. Therefore, it's required to find an alternative conductive matrix to achieve ohmic contacts and strong interactions between conductive matrix and active species.

MXenes, an emerging family of 2D transition metal carbides and nitrides[31], have attracted great attention in the applications of supercapacitors, lithium (sodium)-ion batteries, lithium-sulfur batteries, and catalysis, due to their dominant combinations of properties such as excellent electronic conductivity, tunable interlayer spacing, hydrophilicity, and good mechanical flexibility[9, 32-41]. Notably, the conductivity of solution-dispersable $Ti_3C_2T_x$ MXene is measured to be around 6.76×10^5 S/m, surpassing the solution-processed graphene films[42, 43]. Therefore, the highly conductive $Ti_3C_2T_x$ MXene can be served as an excellent matrix to couple with TMCs, boosting the transport kinetics of ions and electrons by reducing the contact resistance and enhancing the interaction at the contact interfaces. Recently, Liu et al. assembled transition metal oxides (e.g., TiO_2, SnO_2) on the MXene nanosheets through van der Waals interactions. The composites exhibited superior high-rate performance as LIBs anode materials. In those hybrid materials, the MXene nanosheets not only prevent transition metal oxides from aggregation during charge/discharge processes but also accelerate electron and ion transport at the contact interface.[41] In another study, Ma et al. synthesized few layered MoS_2 into Ti_3C_2 interlayer nanospace through electrostatic attraction and cetyltrimethyl ammonium bromide (CTAB) intercalation, which also achieved fast and stable Li/Na storage performance.[9]

Inspired by the abovementioned structural design strategies, in this work, we first employed Co-MOF as precursor to construct the hollow sphere decorated by $CoSe_2$ nanoparticles embedded within the porous carbons. And then negatively charged MXene nanosheets are uniformly coated on the positively charged $CoSe_2$ hollow sphere though electrostatic self-assembly method. It was demonstrated that strong chemical interactions are formed between $CoSe_2$ sphere and MXene flakes, which could considerably accelerate ion/electron-transport

kinetics. Furthermore, the MXene nanosheets coated on the $CoSe_2$ hollow spheres are beneficial for reinforcing the composite structure, preventing the hollow structure from collapse and further improving the composite durability. As a result, the as-obtained $CoSe_2$@MXene hybrids achieve significantly enhanced lithium storage properties.

2. Experimental

Synthesis of Co-MOF: In a typical synthesis, two solutions were first prepared by dissolving 10 mmol of $Co(NO_3)_2 \cdot 6H_2O$ and 14.6 mmol of 1,3,5-benzenetricarboxylic acid in 100 mL of methanol, respectively. Then, the solution of 1,3,5-benzenetricarboxylic acid was quickly poured into the solution of $Co(NO_3)_2 \cdot 6H_2O$, and the resultant mixed solution was stirred for 10 h at room temperature. The obtained mixture was transferred into a 250 mL of Teflon-lined stainless-steel autoclave and heated at 180 °C for 24 h. After natural cooling to room temperature, the violet precipitate was centrifuged and washed thoroughly with methanol and N,N-Dimethylformamide for several times. The obtained product was dried at 80 °C for 24 h under vacuum.

Synthesis of $CoSe_2$ hollow sphere: The as-prepared Co-MOF was mixed with selenium power with a mass ratio of 1:4. The mixture was heated at 600 ^oC for 4 h with a heating rate of 2 ^oC min^{-1} in argon atmosphere to obtain $CoSe_2$ hollow sphere. The mass loading of $CoSe_2$ in MOF-derived $CoSe_2$ hollow sphere was calculated to be 79.55 wt.% (Figure S2).

For comparison, pure $CoSe_2$ was synthesized by hydrothermal method. In a typical procedure, 1.0 g $Co(NO_3)_2 \cdot 6H_2O$ was dissolved in 150 mL of deionized water to form pink solution. 0.542 g Se was then added into the above solution. After stirring for 2 h, 15 mL of hydrazine hydrate ($N_2H_4 \cdot H_2O$, 50%) solution was added into the mixture. After further stirring for 0.5 h, the above solution was

transferred into a 250 mL of Teflon-lined autoclave. The autoclave was tightly sealed and maintained at 180 °C for 24 h and then naturally cooled to room temperature. The resulting product was collected and washed thoroughly with deionized water and ethanol for several times. Then, the obtained black powder was dried at 80 °C for 12h under vacuum. Finally, the product was heated at 600 ^{o}C for 1 h with a heating rate of 2 ^{o}C min^{-1} in argon atmosphere to obtain pure $CoSe_2$.

Synthesis and delamination of $Ti_3C_2T_x$: In a typical procedure, 0.5 g of lithium fluoride (LiF) was added to 10 mL of HCl (6.0 M), and stirred for 10 min. Then, 0.5 g of Ti_3AlC_2 powder was slowly added into the mixture in a course of 10 min to avoid overheating. The reaction mixture was kept at 35 °C for 24 h under magnetic stirring, after which the reaction mixture was washed with distilled water, centrifuged (3500 rpm) until the pH of the supernatant reached approximately 6. The precipitate was dispersed in distilled water by sonication in argon atmosphere for 1 h in the ice-water bath, and dark green supernatant was obtained by centrifugation at 3500 rpm for 1 h. Finally, the MXene nanosheets were obtained by freezedrying under vacuum for 3 days to sublimate the frozen solvent.

Synthesis of $CoSe_2$@MXene hybrid spheres: Typically, 500 mg of $CoSe_2$ hollow spheres and 50 mg of PDDA were dispersed into 100 mL of deionized water with magnetic stirring for 12 h. Then, $CoSe_2$-PDDA suspension was slowly added into 112 mL of $Ti_3C_2T_x$ MXenes suspension (0.5 mg mL^{-1}) by magnetic stirring for 24 h. After that, the mixture was placed in a freeze dryer under vacuum. Finally, the product was annealed at 700 °C for 1 h at a heating rate of 5 °C min^{-1} under argon atmosphere to obtain $CoSe_2$@MXene hybrid spheres.

3. Characterization

Material Characterizations: Crystal structure of samples were characterized using X-ray powder diffraction (XRPD; D8 Advance, Bruker AXS) equipped with Cu Kα radiation (λ = 1.5406). The microstructure and morphology of samples were characterized using transmission electron microscope (TEM, JEOL 2011 F) coupled with an EDX spectrometer, fieldemission scanning electron microscope (FESEM, GeminiSEM 500). BET specific surface area and porosity were determined using an adsorption analyzer (Micromeritcs ASAP 2020). Thermogravimetic analysis (TGA, Netzsch STA 449 F3) were analyzed in an air atmosphere at the heating rate of 10 °C min^{-1}. The element chemical states were dectected by the X-ray energy disperse spectrometry equipped with an Al Kα radiation source (XPS, Thermo ESCALAB 250Xi).

Electrochemical Measurements: The electrochemical tests were carried out in coin-cell configurations (CR2032) at room temperature. The working electrodes consist of active materials (80 wt %), carbon black (10 wt %), and poly(vinylidene fluoride) (10 wt %). The obtained homogeneous slurry was evenly pasted onto Cu foil and dried at 100 °C for 12 h under vacuum. The mass loading was around 1.0 mg cm^{-2}. Pure Li foil was used as counter electrode, and the separator was a polypropylene membrane (Celgard 2400). The electrolyte was 1 mol L^{-1} LiPF6 in a mixture of propylene carbonate (PC), ethylene carbonate (EC), and diethyl carbonate (DEC) (1:4:5 in volume). CR2032 coin half cells were fabricated in an Ar-filled glovebox. CV measurements were performed in a voltage range of 0.01-3.0 V by using CHI 760E electrochemical workstation (Shanghai CH Instrument Co., Ltd.) at room temperature. The galvanostatic charge/discharge measurements were conducted with a multichannel battery testing system (CT2001A, LAND). The impedance spectra

was recorded on constant voltage mode over the frequency range from 100 kHz to 0.01 Hz.

Computational Details: Density functional theory (DFT) calculations were carried out using projector-augmented wave (PAW) method as implemented in Vienna ab initio simulation package (VASP)[44-46]. A generalized gradient approximation (GGA) of Perdew-Burke-Ernzerhof (PBE) functional was employed to describe the exchange-correlation interaction[47]. An energy cutoff of 500 eV and 3×3×1 k-points mesh were applied to all calculations. The structures were relaxed until the forces and total energy on all atoms were converged to less than 0.05 eV $Å^{-1}$ and 1×10^{-5} eV. The charge difference plots are obtained by subtracting the charge densities of pristine O-Ti_3C_2 and isolated $CoSe_2$ molecule from that of $CoSe_2$ adsorbed O-Ti_3C_2.

To evaluate the adhesive strength of $CoSe_2$, the binding energy (E_b) was calculated for every $CoSe_2$ adsorbed compound. E_b was defined as the energy difference before and after $CoSe_2$ adsorption,

$$E_b = E_{Total} - E_{CoSe_2} - E_{substrate}$$

where $E_{substrate}$ and E_{Total} are the total energy of pristine and $CoSe_2$ adsorbed O-Ti_3C_2, respectively. E_{CoSe_2} is the energy for $CoSe_2$ molecule. Therefore, a lower value of E_b indicates a stronger adsorption interaction.

3. Results and discussion

The preparation procedures of $CoSe_2$@MXene hollow spheres are illustrated in Figure 1. In the first step, uniform Co-based metal organic framework spheres are facilely synthesized by a solvothermal method. The collected porous Co-MOF spheres are uniformly mixed with Se powder, and then annealed at 600 °C in argon atmosphere. During this process, hollow spheres with $CoSe_2$ nanoparticles-embedded carbon shell are obtained due to the Kirkendall effect[6,

[25], in which the different diffusion rates of Co and Se result in the formation of hollow structure. In order to obtain a uniform composite of $CoSe_2$@MXene hybrids, we combined the two components by electrostatic self-assembly rather than random physical mixing. Specifically, the $CoSe_2$ hollow spheres were modified by poly(diallyldimethylammonium chloride) (PDDA) to render the $CoSe_2$ surface positively charged. After then, the PDDA-functionalized cobalt selenide spheres (denoted as $CoSe_2$-PDDA) were mixed with $Ti_3C_2T_x$ MXene colloidal solution. The MXene nanosheets are negatively charged due to the presence of the surface polar functional groups (e.g. -O, -F, and -OH).[38, 39] Consequently, the MXene flakes were spontaneously assembled on the surface of $CoSe_2$-PDDA hollow spheres through electrostatic interactions. Finally, the $CoSe_2$@MXene hybrids were obtained after thermal treatment to remove the residual PDDA and surface functional groups, and enhance the stability and crystallinity of the product. For comparison, pure $CoSe_2$, and $CoSe_2$ hollow spheres were also fabricated.

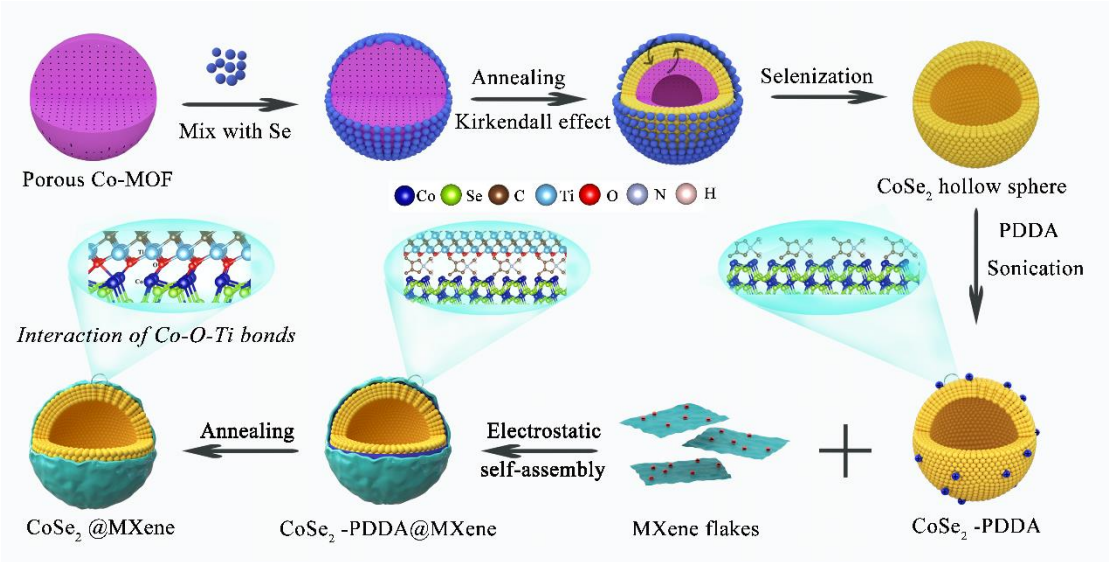

Figure 1. Schematic of the preparation of $CoSe_2$@MXene hybrids.

The FESEM image of as-prepared Co-MOF (Figure S1a) shows that Co-MOF consists exclusively of uniform microspheres with an average particle-size of

around 3-4 um. The magnified FESEM image reveals the porosity of the inner structure in Co-MOF and the smooth surface of microspheres. After further selenization, the Co-MOF spheres are chemically converted into $CoSe_2$ microspheres with the same size, exhibiting rough surface with embedded $CoSe_2$ nanoparticles ranging from 60 to 80 nm (Figure 2a, b). The hollow interior of $CoSe_2$ sphere can be distinctly identified from the cracked microsphere (Figure 2c). The shell of hollow microsphere with a thickness of around 500 nm, exhibits porous structure decorated with $CoSe_2$ nanoparticles (Figure 2c). Specifically, upon the selenization process, the reaction between Co and Se is mainly occurred on the external surface of microspheres, owing to the higher diffusion rate of cobalt species and lower diffusion rate of selenium. As a result, the hollow sphere interior and the carbon enriched outer shell decorated with $CoSe_2$ nanoparticles are eventually obtained. As exhibited in Figure 2d, after coated by MXene sheets, the $CoSe_2$@MXene microspheres present smooth surface without coarse particles, which is further confirmed by the magnified FESEM as shown in Figure 2e. It indicates that the $Ti_2C_3T_x$ MXene nanosheets, are uniformly, tightly, and dispersedly encapsulated on the surface of $CoSe_2$ spheres. The elemental mapping images (Figure 2j) based on SEM image show uniform distribution of the Co, Se, Ti, and C elements in the composite, further indicating the homogeneous encapsulation of MXene on the $CoSe_2$ microspheres.

Transmission electron microscopy (TEM) results show that the hollow interior of $CoSe_2$@MXene microspheres can be definitely observed by the striking contrast between the inner cavity and outer shell (Figure 2f), and the hollow spheres consist of $CoSe_2$ nanoparticles with an average particle-size of 60-80 nm (Figure 2g). These nanoparticles are tightly coated by MXene flakes with a thickness of around 5 nm (Figure 2h), which can act as three-dimensional

conductive network to connect each $CoSe_2$ nanoparticle on the surface of spheres. The high resolution TEM (HRTEM) image further reveals the lattice fringes with a lattice spacing of 0.293 nm, attributing to the (200) plane of cubic $CoSe_2$, which is consistent with the XRD results (Figure 3a). The selected area electron diffraction (SAED) pattern (Figure 2i) indicates that $CoSe_2$ nanoparticle is single crystalline and the diffraction dots belong to (211), (200), (210), (311), (321), and (023) planes of $CoSe_2$.

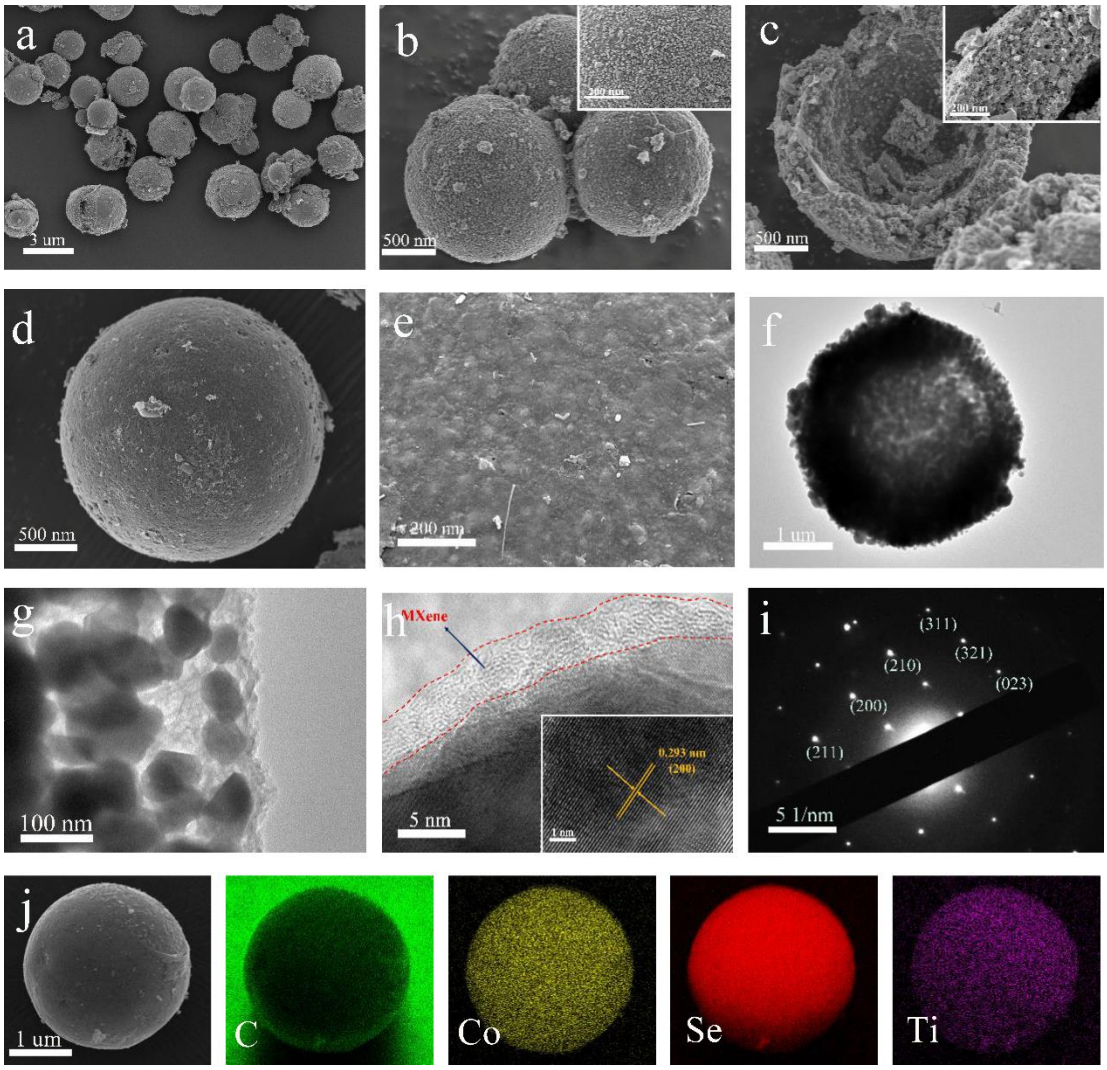

Figure 2. (a-c) FESEM images of the $CoSe_2$ hollow microspheres at different magnifications. (d, e) FESEM images, (f-g) TEM images, (h) HRTEM image, (i) SAED images, (j) SEM image and corresponding elemental mapping images of C, Co, Se, and Ti elements of the $CoSe_2$@MXene.

Figure 3a shows the XRD patterns of $CoSe_2$@MXene, $CoSe_2$ spheres and MXene, respectively. The $CoSe_2$@MXene shows combined phases of cubic pyrite $CoSe_2$ (JCPDS no. 65-3327; space group Pa-3(205), a = b = c=5.859 Å) and exfoliated $Ti_3C_2T_x$ MXene. The narrow half-peak width indicates the high crystallinity of $CoSe_2$, and no impurity peaks observed imply the high purity of the products.

The N_2 adsorption-desorption measurement was employed to evaluated the porous feature of $CoSe_2$@MXene hybrids, as presented in Figure 3b. Notably, the typical hysteresis loops could be observed, indicating the presence of mesoporous in the samples. The $CoSe_2$@MXene spheres possess a specific surface area of 63.45 m^2/g, and a pore volume of 0.104 cm^3/g at P/P_0 = 0.999. Meanwhile, the pore size distribution further demonstrated the mesoporous structure ranging from 2 to 50 nm, which was in accordance with N_2 adsorption isotherms. The hierarchical porous structure with large specific surface area, appropriate pore volume, and mesoporous feature, is beneficial to facilitate the diffusion of lithium ions and electron transfer as well as electrolyte infiltration. Moreover, the porous structure could provide enough space to buffer the large volume variation during repeated Li-ion insertion/desertion, contributing to enhanced electrochemical performance.

The survey X-ray photoelectron spectroscopy (XPS) spectrum in Figure S3 shows that the $CoSe_2$@MXene hybrids are composed of C, O, Co, Se, and Ti elements. Specifically, in the Co 2p spectrum (Figure 3c), the peaks at 796.5, 793.1, 781, and 778.15 eV are ascribed to the Co-Co and Co-Co of Co 2p1/2, Co-O and Se-Co-Se of Co 2p3/2, respectively.[22, 24, 48, 49] In addition, the peaks located at 802.3 and 785.05 eV are related to satellite peaks.[24] As exhibited in Figure 3d, the Se 3d XPS region can be deconvoluted into three dominant peaks

at 55.8, 56.6, and 59.4 eV, which are assigned to Co-Se, Se-Se, and Se-O, respectively.[22, 24] In O 1s spectrum (Figure 3e), except for the peaks ascribed to Ti-C-$(OH)_x$ and Ti-C-O_x[41, 50-52], a strong signal peak at 529.1 eV is noticed for the $CoSe_2$@MXene sample, implying the generation of strong covalent bond interactions at the interface between $CoSe_2$ and Ti_2C_3 MXene. The Co-O-Ti bonds are formed by bonding Co atoms of $CoSe_2$ and surface oxygen-containing functional groups of MXene, dramatically enhancing the interactions between the two components. Moreover, in comparison with MXene nanosheets, the peak attributed to Co-O-Ti bonds (461.2 eV) also can be found in the high-resolution Ti 2p (Figure 3f) spectrum[50, 51], further verifying the existence of Co-O-Ti covalent bonds. Similarly, a covalent Ti-O-Mo between $MoSe_2$ and MXene[53], and the Mo-C covalent bond between MoS_2 and MXene[9], have been validated. The strong Co-O-Ti covalent bond interactions are expected to accelerate the electron and ion transport rate, enhance the structural durability of the $CoSe_2$@MXene electrode, and thus improve the LIBs electrochemical performances.

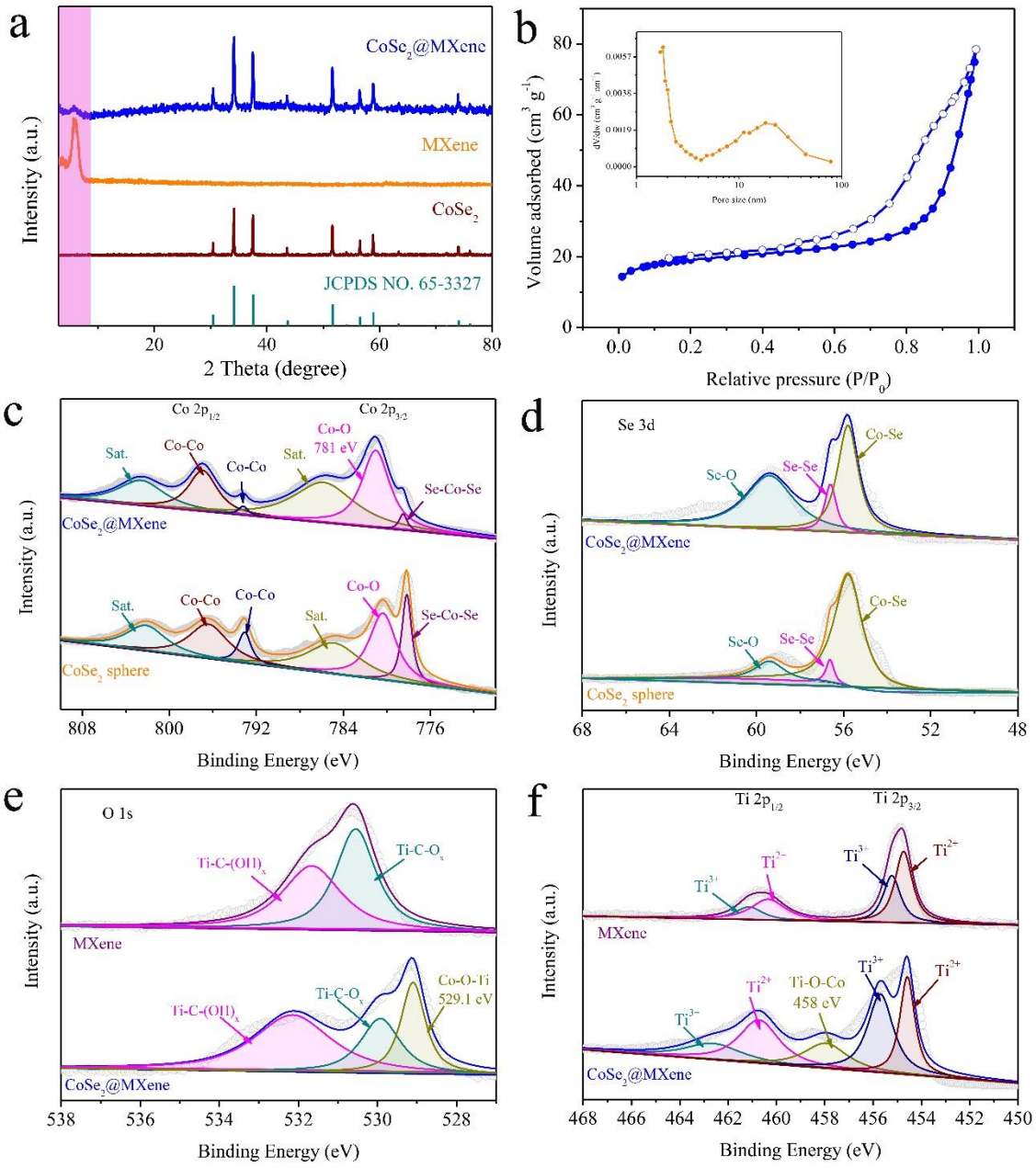

Figure 3. (a) XRD patterns of $CoSe_2$ hollow sphere, Ti_3C_2 MXene and $CoSe_2$@MXene. (b) N_2 adsorption−desorption isotherms and the corresponding pore size distribution (inset) of $CoSe_2$@MXene. High-resolution spectra of (c) Co 2p, (d) Se 3d, (e) O 1s, and (f) Ti 2p of MXene, $CoSe_2$ sphere, and $CoSe_2$@MXene.

As exhibited in Figure 4a, the CV profiles of the $CoSe_2$@MXene hybrids were measured between 0.01 V and 3.0 V (vs Li/Li^+) at a scan rate of 0.1 mV s^{-1}. In

the first cathodic scan, two obvious reduction peaks located at 1.26 and 0.60 V can be observed, which could be ascribed to the conversion from $CoSe_2$ to Li_xCoSe_2, Li_2Se and metallic Co as well as the formation of the SEI layer due to the decomposition of electrolyte.[3, 14, 54] In the subsequent anodic scan, two oxidation peaks at 2.10 and 2.3 V are associated with the oxidation of Co to $CoSe_2$.[3, 14] Starting from the 2rd cycle, the CV curves exhibit three pronounced cathodic peaks and two anodic peaks, where the cathodic peaks shift towards the positive potential. Furthermore, the anodic and cathodic peaks are well overlapped, suggesting the highly reversible process of lithium insertion and extraction. Notably, the charge/discharge plateaus represented by discharge−charge voltage profiles of $CoSe_2$@MXene (Figure 4e) match well with the CV results.

Figure 4b shows that, compared to $CoSe_2$ hollow spheres, and pristine $CoSe_2$, $CoSe_2$@MXene electrodes deliver high capacities of 1051, 856, 763, and 669 mAh g^{-1} at current densities of 200, 500, 1000, and 2000 mA g^{-1}, respectively. Event at a current density of 5 A g^{-1}, a considerable reversible capacity of 465 mAh g^{-1} is still preserved. The high rate performance of $CoSe_2$@MXene is significantly advanced to other reported TMDs anodes for LIBs (Figure S4 and Table S1). Notably, the specific capacity of $CoSe_2$@MXene quickly recovered to 994 mA h g^{-1} with a capacity retention of 95% when scanned again at 200 mA g^{-1}, indicating its remarkable reversibility. Figure 4c exhibited typical charge−discharge profiles of the $CoSe_2$@MXene hybrids at different current densities. With the current density increased, the voltage gap became gradually wider and the plateaus as well as slopes were apparently remained, further indicating the excellent rate performance of $CoSe_2$@MXene.

The cycling performance of $CoSe_2$@MXene electrodes at a current density of 0.2 A g^{-1} over 100 cycles is shown in Figure 4d. Compared to pure $CoSe_2$ and $CoSe_2$ hollow sphere, $CoSe_2$@MXene electrodes exhibit superior cycling property, delivering a reversible capacity as high as 910 mAh g^{-1} after 100 cycles with a capacity retention of 92.19%. Correspondingly, the capacity decay is only 0.078% per cycle calculated from the 5th cycle. After the first few cycles, the ultrahigh Coulombic efficiency of approximate 99% was obtained in the subsequent cycles. For comparison, $CoSe_2$ hollow sphere delivers a capacity of 484 mAh g^{-1}, whereas pure $CoSe_2$ only exhibits 86 mAh g^{-1} after 100 cycles. Distinctly, these results demonstrate that the structural superiority of $CoSe_2$@MXene hybrids, combining the hollow structure and MXene conductive matrix, could dramatically enhance their lithium storage performance as expected. The corresponding charge/discharge curves of $CoSe_2$@MXene at 0.2 A g^{-1} are presented in Figure 4e, further demonstrating the excellent cycling performance. Impressively, the $CoSe_2$@MXene electrodes exhibit an initial discharge capacity of 1320 mAh g^{-1} and a charge capacity of 949 mAh g^{-1}, corresponding to a high initial Coulombic efficiency (ICE) of 71.9%. This high value outperforms that of many TMCs, attributing to the structural features of $CoSe_2$@MXene, in which the hollow spheres decorated with electroactive $CoSe_2$ nanoparticles are tightly coated by MXene flakes.

The long-term cycling performance of the $CoSe_2$@MXene, $CoSe_2$ spheres, and pure $CoSe_2$ electrodes were evaluated over 1000 cycles at a current density of 1 A g^{-1} (Figure 4f). Interestingly, both $CoSe_2$@MXene and $CoSe_2$ spheres electrodes exhibit a capacity rise phenomenon during the long-term cycles. Specifically, the $CoSe_2$@MXene electrode exhibits a stable capacity of approximately 835 mAh g^{-1} before 300th cycles. Then, the capacity gradually

increases to a stable value as high as 1279 mAh g^{-1} after 1000 cycles, which is far superior to that of pure $CoSe_2$ (34.8 mAh g^{-1}), $CoSe_2$ spheres (388 mAh g^{-1}), and most previously reported TMCs. Meanwhile, the specific capacity of $CoSe_2$ spheres electrode slightly increases from 438 mAh g^{-1} (300th cycle) to 480 mAh g^{-1} (500th cycle). The capacity climbing phenomenon of $CoSe_2$@MXene and $CoSe_2$ spheres electrodes, which is quite common for many conversion reaction type materials, is possibly associated with the reversible formation of a polymeric gel-like layer, as well as the activation process of the active species.[25, 55, 56] During the cycle process, the reversible formation and decomposition of the polymeric-gel-like film could deliver excess capacity through a "pseudo-capacitance-type behavior".[57, 58]

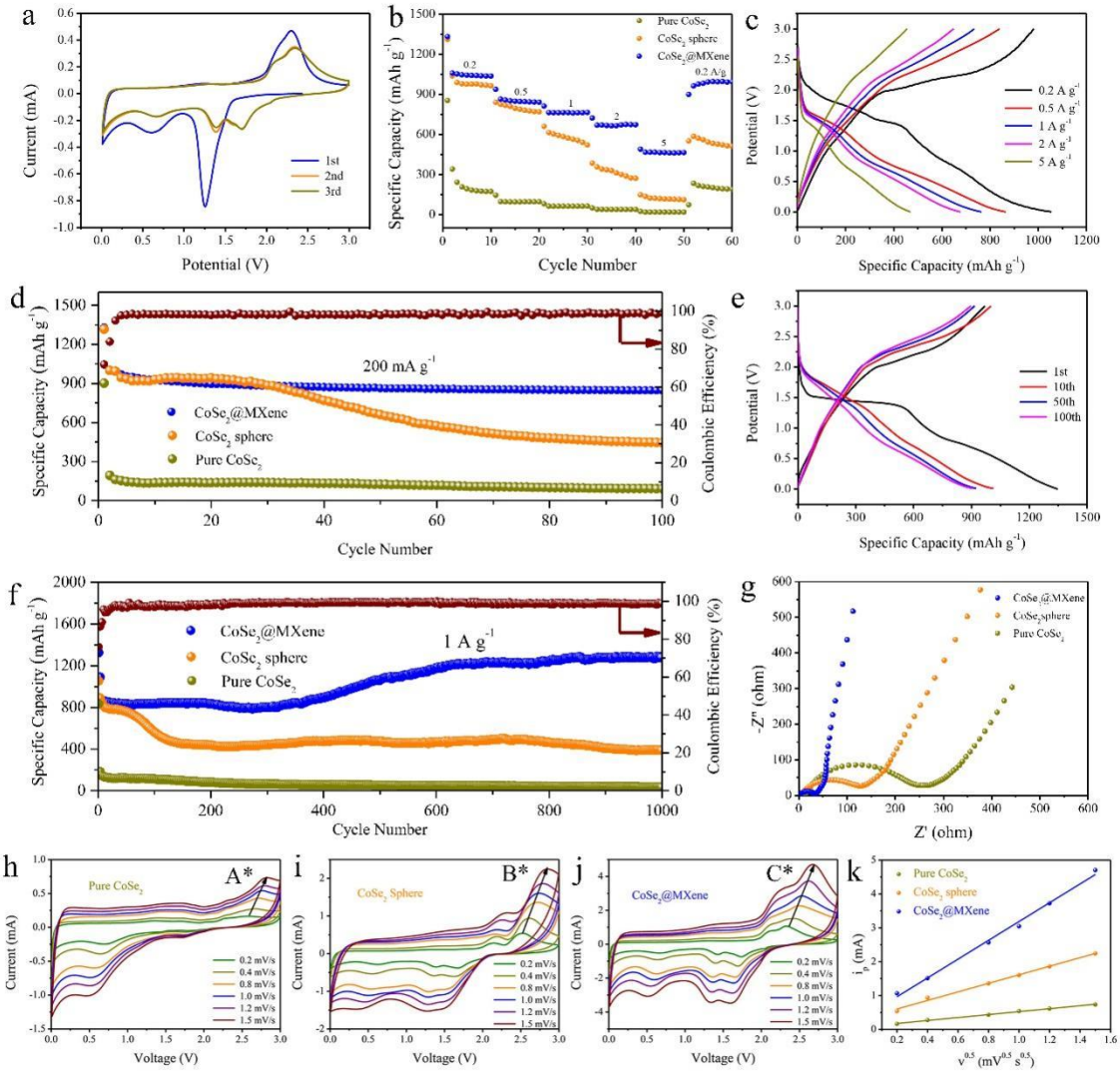

Figure 4. (a) CV curves of $CoSe_2$@MXene at a scan rate of 0.1 mV s^{-1}. (b) Comparison of rate performance of $CoSe_2$@MXene, $CoSe_2$ sphere, and pure $CoSe_2$ at various current densities. (c) The charge/discharge profiles of $CoSe_2$@MXene at various rates. (d) Comparison of cycling performance of $CoSe_2$@MXene, $CoSe_2$ sphere, and pure $CoSe_2$ at 200 mA g^{-1}. (e) Galvanostatic discharge and charge curves of $CoSe_2$@MXene at a current rate of 200 mA g^{-1}. (f) Cycling performance of as-prepared electrodes 1 A g^{-1}. (g) Nyquist plots of pure $CoSe_2$, $CoSe_2$ sphere and $CoSe_2$@MXene electrodes. CV curves at different scan rates of (h) pure $CoSe_2$, (i) $CoSe_2$ sphere, and (j) $CoSe_2$@MXene. (k) Linear relationship of peak currents versus $mV^{0.5} \cdot s^{-0.5}$ and the corresponding linear

fits for pure $CoSe_2$, $CoSe_2$ sphere and $CoSe_2$@MXene electrodes. The data of peak currents are extracted from A* in Figure 4h, B* in Figure 4i, and C* in Figure 4j.

Furthermore, to have insight into the electrochemical kinetics, electrochemical impedance spectra (EIS) curves of $CoSe_2$@MXene, $CoSe_2$ spheres, and pure $CoSe_2$ were measured and the corresponding equivalent circuit model was fitted (Figure 4g and S6). The Nyquist plot of $CoSe_2$@MXene electrode shows much smaller semicircle at the high and middle frequencies, implying a better electronic conductivity, smaller contact resistance, and lower charge-transfer resistance. The corresponding charge-transfer resistance (R_{ct}) for $CoSe_2$@MXene, $CoSe_2$ spheres, and pure $CoSe_2$ are 14.7 Ω, 63.2 Ω and 230.5 Ω, respectively. Moreover, $CoSe_2$@MXene exhibits a straight line with higher slope, indicating fast Li ions diffusion during the lithiation/delithiation process. To further fully elucidate the electrochemical kinetics of $CoSe_2$@MXene, the CV curves at different scan rates ranging from 0.2 to 1.5 mV s^{-1} were analyzed (Figure S5a). The CV curves exhibit similar peaks, where three cathodic peaks and two anodic peaks could be distinctly found. The relationship between current response (i) and the sweep rate (v) obeys the following equations:[6, 12, 53]

$$i = av^b \quad (1)$$

$$\log(i) = b\times\log(v) + \log(a) \quad (2)$$

where the b value of 0.5 represents diffusion-controlled behavior and 1.0 indicates pseudocapacitive process.[9] As displayed in Figure S5b, the b-values of the three cathodic peaks (peaks 1, 2 and 3) and the corresponding anodic peaks (peaks 4 and 5) were determined to be 0.75, 0.85, 0.88, 0.71, and 0.83, respectively, manifesting that the Li^+ storage kinetics of $CoSe_2$@MXene consisted partial pseudocapacitive behaviors, and thus contributing to fast Li^+

interaction/extraction process featured by outstanding rate performance. The pseudocapacitive contributions can be calculated by the following equation:[3, 9]

$i = k_1v + k_2v^{1/2}$ (3)

where k_1v and $k_2v^{1/2}$ correspond to pseudocapacitance contribution and diffusion contribution, respectively. Specifically, the pseudocapacitive fraction reaches a value as high as 80.6% at 1.5 mV/s (Figure S5c). With the sweep rate increased, the ration of pseudocapacitive contribution gradually becomes higher (Figure S5d), suggesting that pseudocapacitance dominates the charge/discharge process at high sweep rate. The pseudocapacitive behavior may profit from the hierarchical 3D hollow architecture with a large surface and much sites, which contributes to superior rate performance of $CoSe_2$@MXene.

Moreover, the lithium diffusion behaviors of different electrodes were revealed by Randles–Sevcik evaluations. Figure 4h-j present the CV curves of pure $CoSe_2$, $CoSe_2$ sphere, and $CoSe_2$@MXene at scan rates ranging from 0.2 to 1.5 mV/s. As the scan rate increasing, the cathodic peaks would shift progressively to lower potential while the anodic peaks shift towards higher potential, with an augment in the peak intensity, and the shapes of CV curves remain similar at different scan rates. This phenomenon associates with the rate of electrochemical reaction, which are highly lied on the lithium-ion diffusion process.[59] The Li^+ diffusion coefficients (D_{Li^+}) of pure $CoSe_2$, $CoSe_2$ sphere, and $CoSe_2$@MXene electrodes are assessed by the Randles-Sevcik equation:[59]

$$i_p = 0.4663nFAC_0\sqrt{\frac{nFDv}{RT}} \quad (4)$$

In this equation: i_p, n, C_0, A, D, and v represent to the peak current in the CV curves, the number of electrons, the concentration of Li^+, the surface area of the electrodes, the diffusion coefficient, and the potential scan rate, respectively. R,

T and F correspond to the gas constant, the absolute temperature during the CV measurement, and the Faraday constant, respectively. Since the CV test of electrodes and the fabrication of cells are under the same condition, the Randles-Sevcik equation to evaluate diffusion coefficient could be simplified as:[59]

$$i_p = k\sqrt{D}\sqrt{v} \qquad (5)$$

In which, k is regarded as a constant due to the same measurement condition, and thus, the lithium-ion diffusion coefficient (D_{Li^+}) could be redefined as $kD^{1/2}$. Therefore, the value of D_{Li^+} could be reflected by the linear relationship between i_p and $v^{1/2}$. As clearly presented in Figure 4k, $CoSe_2$ sphere presents faster Li^+ diffusion rate than that of pure $CoSe_2$, attributing to its hollow, porous, and conductive structure. Moreover, the incorporation of MXene coated on the surface of $CoSe_2$ sphere could further accelerate the lithium-ion diffusion kinetics of $CoSe_2$@MXene. As results, the pure $CoSe_2$ and $CoSe_2$@MXene electrodes show more superior electrochemical performances.

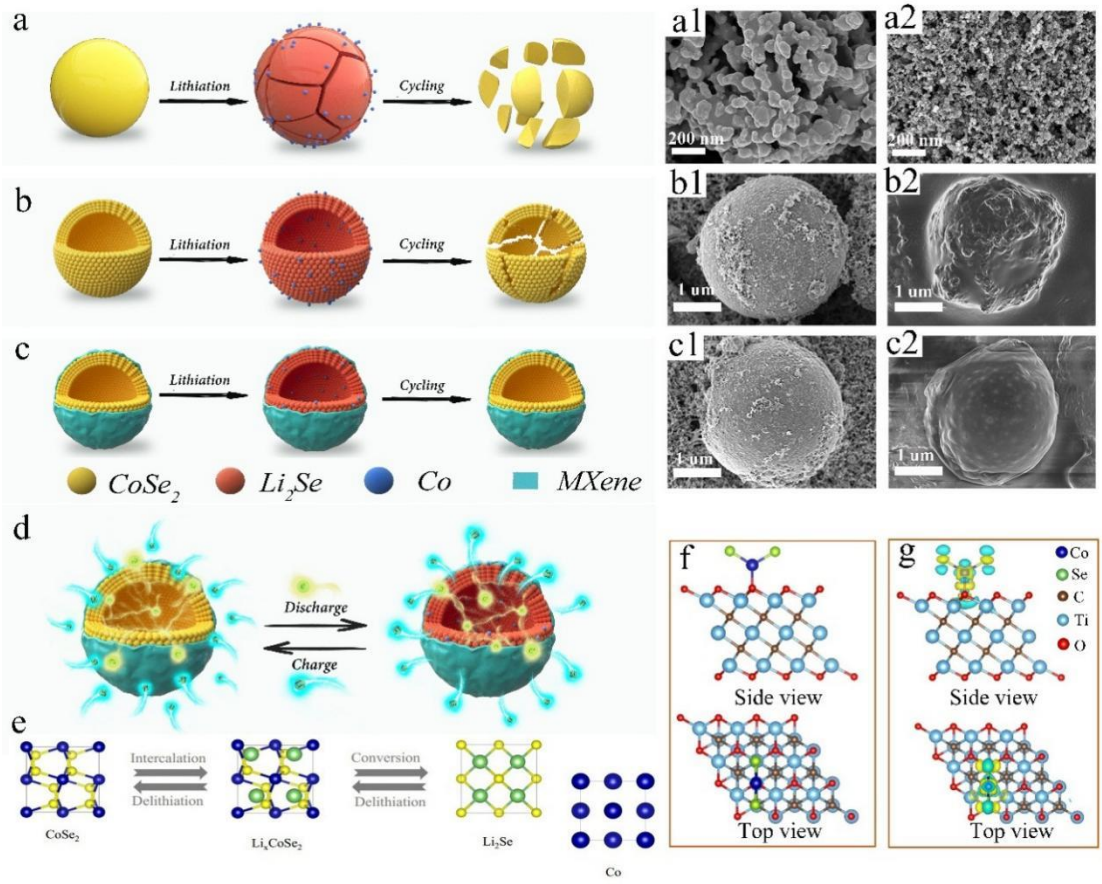

Figure 5 Schematic of the structural stability of (a) pure $CoSe_2$ electrode, (b) hollow $CoSe_2$ spheres electrode, and (c) $CoSe_2$@MXene electrode, during the repeated cycles. The FESEM images of (a_1 and a_2) pure $CoSe_2$ electrode, (b_1 and b_2) hollow $CoSe_2$ spheres electrode, and (c_1 and c_2) $CoSe_2$@MXene electrode in various state: (a_1, b_1, and c_1) initial state, (a_2, b_2, and c_2) after 1000 cycles at 1 A g^{-1}. (d) Schematic illustration of the reversible lithium storage process of the $CoSe_2$@MXene electrode. (e) The crystal structures transformation during lithiation/delithiation process for $CoSe_2$. (f) Adsorption configuration and (g) charge density difference of $CoSe_2$ adsorbed O-Ti_3C_2. The C, Ti, O, Co and Se atoms are depicted in brown, wathet, red, dark blue and green, respectively. Areas of charge accumulation are shown in yellow while depletion are shown in blue.

To further understand the relationship between the electrochemical performance and the stability of the morphology and structure of $CoSe_2$@MXene, the morphology of all the samples before cycles and after 1000 cycles at 1 A g^{-1} has

been analyzed. As shown in Figure 5c_1-c_2, compared with initial state, the hollow $CoSe_2$@MXene microsphere maintains good structural integrity without obvious morphology damage. This can be ascribed to the hollow structure, providing adequate space to cushion the volume expansion during cycles, and the coated MXene flakes, which could enhance the structural durability through the formation of the Ti-O-Co bonds. However, without the protection of MXene flakes, hollow $CoSe_2$ microsphere suffers from slight cracks and collapse, in which the hollow structure plays a positive role in preventing the severe structural damage (Figure 5b_1-b_2). Even worse, the pure $CoSe_2$ electrode is subjected to serious pulverization along cycling (Figure 5a_1-a_2), due to the huge volume change during lithiation/delithiation, resulting in inferior cycling stability and rate performance. Figure 5a-c illustrate the structure evolution of pure $CoSe_2$, hollow $CoSe_2$ microsphere, and hollow $CoSe_2$@MXene microsphere anodes for LIBs during the cycling process, fully demonstrating the superiority of the rational and robust architecture of $CoSe_2$@MXene.

Furthermore, density functional theory (DFT) calculations are performed to verify the chemical interaction between $CoSe_2$ and oxygen functionalized Ti_3C_2 (denote as O-Ti_3C_2). As presented in Figure 5f, the most stable geometrical configuration with a binding energy of -2.18 eV is formed, when $CoSe_2$ molecule is adsorbed on the O-Ti_3C_2 with Co atom locating at the top of O atom, indicating that the adsorption between $CoSe_2$ and O-Ti_3C_2 MXene is favorable thermodynamically. Moreover, insight into this strong binding interaction is analyzed from the point of view of electronic structure. The charge density difference map (Figure 5g) illustrates the charge redistribution of $CoSe_2$ adsorbed O-Ti_3C_2. The electron accumulation between Co and O atom suggests the formation of Co-O-Ti covalent bond, which is consistent with XPS analysis.

Hence, the formation of strong Co-O-Ti bond, at the interface of $CoSe_2$ and O-Ti_3C_2 MXene, could enhance the structural durability as well as accelerate the electrons and ions transport at the interface, accordingly leading to enhanced rate performance and cycling stability.

According to the above discussion, the outstanding cycling stability and ultrahigh rate capacity of the $CoSe_2$@MXene could be mainly attributed to the rational and robust architecture, constructing by coupling the hollow structure with the highly conductive MXene coating. The hollow structure, efficiently accommodating the mechanical strain induced by huge volume changes, could assure a long-term cycling stability. Moreover, the highly conductive, mechanical flexible, and good adhesive MXene nanosheets exhibit three-fold roles. First, the MXene flakes coated on the surface of hollow $CoSe_2$ microspheres act as "protective film", preventing the hollow structure from damage during the repeated charge/discharge process, which could assuringly exert better function of the hollow structure. Second, the highly conductive matrix of MXene flakes ensure fast electrons transport in the whole electrode, directly reflecting by the low charge-transfer resistance obtained from EIS curves. Third, the formation of strong Ti-O-Co covalent bonds, at the interface of oxygen functionalized Ti_3C_2 MXene and $CoSe_2$, endow the $CoSe_2$@MXene hybrids with a durable structure for long-term cycling, and could accelerate the transport kinetics of electrons and ions between $CoSe_2$ and MXene. The incorporation of MXene nanosheets could dramatically solve the interface issue between two components. Thus, as schematically illustrated in Figure 5d-e for the lithiation/delithiation process, the $CoSe_2$@MXene hybrids exhibit excellent rate performance, ultrahigh reversible specific capacity, and superior cycling stability.

4. Conclusions

In summary, hybrid $CoSe_2$@MXene robust structures, comprised of inner hollow $CoSe_2$ microspheres and outer MXene flakes coating, have been fabricated by a facile electrostatic self-assembly method. The as-obtained $CoSe_2$@MXene hybrids can achieve the strong coupling of high capacity $CoSe_2$ hollow spheres and highly conductive MXene flakes. The hollow spheres structure of $CoSe_2$ is able to accommodate the volume expansion during lithiation/delithiation cycles, while the incorporation of MXene nanosheets could reinforce the composite structure and accelerate ion/electron-transport kinetics. Accordingly, the $CoSe_2$@MXene hybrids deliver an admirable reversible capacity of 1051 mAh g^{-1} at 200 mA g^{-1}, a superior rate capability of 465 mAh g^{-1} at 5 A g^{-1}, and an excellent long-term cycle property at 1 A g^{-1} with a capacity of 1279 mAh g^{-1} after 1000 cycles. The present hollow structure coated by MXene strategy provides an effective route for designing new anode materials.

Conflicts of interest

There are no conflicts to declare.

Acknowledgements

This work was partially supported by the National Key Research and Development Program of China (2017YFA0204600), the National Natural Science Foundation of China (51971065, 51773060, 51625102,), the Innovation Program of Shanghai Municipal Education Commission (2019-01-07-00-07-E00028), and the Science and Technology Commission of Shanghai Municipality (17XD1400700), the International Collaboration Research Program of Science and Technology Commission of Shanghai (16520722000) and Shanghai Natural Science Foundation (16ZR1407700). Zhenguo Huang is grateful for the financial support from ARC (DP170101773).

References

1. Dunn, B.; Kamath, H.; Tarascon, J., Electrical Energy Storage for the Grid: A Battery of Choices. *Science* **2011**, 334 (6058), 928-935.

2. Etacheri, V.; Marom, R.; Elazari, R.; Salitra, G.; Aurbach, D., Challenges in the development of advanced Li-ion batteries: a review. *Energy & Environmental Science* **2011,** 4, (9).

3. Yang, J.; Gao, H.; Men, S.; Shi, Z.; Lin, Z.; Kang, X.; Chen, S., $CoSe_2$ Nanoparticles Encapsulated by N-Doped Carbon Framework Intertwined with Carbon Nanotubes: High-Performance Dual-Role Anode Materials for Both Li- and Na-Ion Batteries. *Adv Sci* **2018,** 5, (12), 1800763.

4. Zhang, B.; Xia, G.; Sun, D.; Fang, F.; Yu, X., Magnesium Hydride Nanoparticles Self-Assembled on Graphene as Anode Material for High-Performance Lithium-Ion Batteries. *ACS Nano* **2018,** 12, (4), 3816-3824.

5. Deng, Z.; Jiang, H.; Hu, Y.; Liu, Y.; Zhang, L.; Liu, H.; Li, C., 3D Ordered Macroporous MoS_2 @C Nanostructure for Flexible Li-Ion Batteries. *Adv Mater* **2017,** 29, (10).

6. Zhang, B.; Xia, G.; Chen, W.; Gu, Q.; Sun, D.; Yu, X., Controlled-Size Hollow Magnesium Sulfide Nanocrystals Anchored on Graphene for Advanced Lithium Storage. *ACS Nano* **2018,** 12, (12), 12741-12750.

7. Zhou, J.; Lin, J.; Huang, X.; Zhou, Y.; Chen, Y.; Xia, J.; Wang, H.; Xie, Y.; Yu, H.; Lei, J.; Wu, D.; Liu, F.; Fu, Q.; Zeng, Q.; Hsu, C. H.; Yang, C.; Lu, L.; Yu, T.; Shen, Z.; Lin, H.; Yakobson, B. I.; Liu, Q.; Suenaga, K.; Liu, G.; Liu, Z., A library of atomically thin metal chalcogenides. *Nature* **2018,** 556, (7701), 355-359.

8. Zhang, S.; Wang, G.; Jin, J.; Zhang, L.; Wen, Z.; Yang, J., Robust and Conductive Red $MoSe_2$ for Stable and Fast Lithium Storage. *ACS Nano* **2018,** 12, (4), 4010-4018.

9. Ma, K.; Jiang, H.; Hu, Y.; Li, C., 2D Nanospace Confined Synthesis of Pseudocapacitance-Dominated MoS_2-in-Ti_3C_2 Superstructure for Ultrafast and Stable Li/Na-Ion Batteries. *Advanced Functional Materials* **2018,** 28, (40).

10. Zhang, Y.; Zhou, Q.; Zhu, J.; Yan, Q.; Dou, S. X.; Sun, W., Nanostructured Metal Chalcogenides for Energy Storage and Electrocatalysis. *Advanced Functional Materials* **2017,** 27, (35).

11. Hu, Z.; Liu, Q.; Chou, S. L.; Dou, S. X., Advances and Challenges in Metal Sulfides/Selenides for Next-Generation Rechargeable Sodium-Ion Batteries. *Adv Mater* **2017,** 29, (48).

12. Zhang, K.; Park, M.; Zhou, L.; Lee, G.-H.; Li, W.; Kang, Y.-M.; Chen, J., Urchin-Like $CoSe_2$ as a High-Performance Anode Material for Sodium-Ion Batteries. *Advanced Functional Materials* **2016,** 26, (37), 6728-6735.

13. Yu, Q.; Jiang, B.; Hu, J.; Lao, C. Y.; Gao, Y.; Li, P.; Liu, Z.; Suo, G.; He, D.; Wang, W. A.; Yin, G., Metallic Octahedral $CoSe_2$ Threaded by N-Doped Carbon Nanotubes: A Flexible Framework for High-Performance Potassium-Ion Batteries. *Adv Sci* **2018,** 5, (10), 1800782.

14. Liu, W.; Shao, M.; Zhou, W.; Yuan, B.; Gao, C.; Li, H.; Xu, X.; Chu, H.; Fan, Y.; Zhang, W.; Li, S.; Hui, J.; Fan, D.; Huo, F., Hollow Ni-$CoSe_2$ Embedded in Nitrogen-Doped Carbon Nanocomposites Derived from Metal-Organic Frameworks for High-Rate Anodes. *ACS Appl Mater Interfaces* **2018,** 10, (45), 38845-38852.

15. Fang, Y.; Yu, X. Y.; Lou, X. W. D., Formation of Hierarchical Cu-Doped $CoSe_2$ Microboxes via Sequential Ion Exchange for High-Performance Sodium-Ion Batteries. *Adv Mater* **2018,** 30, (21), e1706668.

16. Cai, T.; Zhao, L.; Hu, H.; Li, T.; Li, X.; Guo, S.; Li, Y.; Xue, Q.; Xing, W.; Yan, Z.; Wang, L., Stable $CoSe_2$/carbon nanodice@reduced graphene oxide composites for high-performance rechargeable aluminum-ion batteries. *Energy & Environmental*

Science **2018,** 11, (9), 2341-2347.

17. Zheng, Y. R.; Wu, P.; Gao, M. R.; Zhang, X. L.; Gao, F. Y.; Ju, H. X.; Wu, R.; Gao, Q.; You, R.; Huang, W. X.; Liu, S. J.; Hu, S. W.; Zhu, J.; Li, Z.; Yu, S. H., Doping-induced structural phase transition in cobalt diselenide enables enhanced hydrogen evolution catalysis. *Nat Commun* **2018,** 9, (1), 2533.

18. Wang, B.; Wang, Z.; Wang, X.; Zheng, B.; Zhang, W.; Chen, Y., Scalable synthesis of porous hollow $CoSe_2$–$MoSe_2$/carbon microspheres for highly efficient hydrogen evolution reaction in acidic and alkaline media. *Journal of Materials Chemistry A* **2018,** 6, (26), 12701-12707.

19. Zhao, S.; Jin, R.; Abroshan, H.; Zeng, C.; Zhang, H.; House, S. D.; Gottlieb, E.; Kim, H. J.; Yang, J. C.; Jin, R., Gold Nanoclusters Promote Electrocatalytic Water Oxidation at the Nanocluster/$CoSe_2$ Interface. *J Am Chem Soc* **2017,** 139, (3), 1077-1080.

20. Zhang, H.; Wang, T.; Sumboja, A.; Zang, W.; Xie, J.; Gao, D.; Pennycook, S. J.; Liu, Z.; Guan, C.; Wang, J., Integrated Hierarchical Carbon Flake Arrays with Hollow P-Doped $CoSe_2$ Nanoclusters as an Advanced Bifunctional Catalyst for Zn-Air Batteries. *Advanced Functional Materials* **2018,** 28, (40).

21. Yin, H.; Qu, H.-Q.; Liu, Z.; Jiang, R.-Z.; Li, C.; Zhu, M.-Q., Long cycle life and high rate capability of three dimensional $CoSe_2$ grain-attached carbon nanofibers for flexible sodium-ion batteries. *Nano Energy* **2019,** 58, 715-723.

22. Tang, Y.; Zhao, Z.; Hao, X.; Wang, Y.; Liu, Y.; Hou, Y.; Yang, Q.; Wang, X.; Qiu, J., Engineering hollow polyhedrons structured from carbon-coated $CoSe_2$ nanospheres bridged by CNTs with boosted sodium storage performance. *Journal of Materials Chemistry A* **2017,** 5, (26), 13591-13600.

23. Gao, J.; Li, Y.; Shi, L.; Li, J.; Zhang, G., Rational Design of Hierarchical Nanotubes through Encapsulating $CoSe_2$ Nanoparticles into $MoSe_2$/C Composite Shells

with Enhanced Lithium and Sodium Storage Performance. *ACS Appl Mater Interfaces* **2018,** 10, (24), 20635-20642.

24. Huang, Y.; Wang, Z.; Jiang, Y.; Li, S.; Li, Z.; Zhang, H.; Wu, F.; Xie, M.; Li, L.; Chen, R., Hierarchical porous $Co_{0.85}Se$@reduced graphene oxide ultrathin nanosheets with vacancy-enhanced kinetics as superior anodes for sodium-ion batteries. *Nano Energy* **2018,** 53, 524-535.

25. Hu, H.; Zhang, J.; Guan, B.; Lou, X. W., Unusual Formation of CoSe@carbon Nanoboxes, which have an Inhomogeneous Shell, for Efficient Lithium Storage. *Angew Chem Int Ed Engl* **2016,** 55, (33), 9514-8.

26. Wang, S.; Guan, B. Y.; Yu, L.; Lou, X. W. D., Rational Design of Three-Layered TiO_2 @Carbon@MoS_2 Hierarchical Nanotubes for Enhanced Lithium Storage. *Adv Mater* **2017,** 29, (37).

27. Liu, Y.; Yu, X.-Y.; Fang, Y.; Zhu, X.; Bao, J.; Zhou, X.; Lou, X. W., Confining SnS_2 Ultrathin Nanosheets in Hollow Carbon Nanostructures for Efficient Capacitive Sodium Storage. *Joule* **2018,** 2, (4), 725-735.

28. Zhang, J.; Wu, M.; Liu, T.; Kang, W.; Xu, J., Hierarchical nanotubes constructed from interlayer-expanded $MoSe_2$ nanosheets as a highly durable electrode for sodium storage. *Journal of Materials Chemistry A* **2017,** 5, (47), 24859-24866.

29. Niu, F.; Yang, J.; Wang, N.; Zhang, D.; Fan, W.; Yang, J.; Qian, Y., $MoSe_2$-Covered N,P-Doped Carbon Nanosheets as a Long-Life and High-Rate Anode Material for Sodium-Ion Batteries. *Advanced Functional Materials* **2017,** 27, (23).

30. Yu, X. Y.; Hu, H.; Wang, Y.; Chen, H.; Lou, X. W., Ultrathin MoS_2 Nanosheets Supported on N-doped Carbon Nanoboxes with Enhanced Lithium Storage and Electrocatalytic Properties. *Angew Chem Int Ed Engl* **2015,** 54, (25), 7395-8.

31. Anasori, B.; Lukatskaya, M. R.; Gogotsi, Y., 2D metal carbides and nitrides (MXenes) for energy storage. *Nature Reviews Materials* **2017,** 2, (2).

32. VahidMohammadi, A.; Hadjikhani, A.; Shahbazmohamadi, S.; Beidaghi, M., Two-Dimensional Vanadium Carbide (MXene) as a High-Capacity Cathode Material for Rechargeable Aluminum Batteries. *ACS Nano* **2017,** 11, (11), 11135-11144.

33. Lukatskaya, M. R.; Mashtalir, O.; Ren, C. E.; Agnese, Y. D.; Rozier, P.; Taberna, P. L.; Naguib, M.; Simon, P.; Barsoum, M. W.; Gogotsi, Y., Cation Intercalation and High Volumetric Capacitance of Two-Dimensional Titanium Carbide. *Science* **2013**, 341 (6153), 1502-1505.

34. Wu, Y.; Nie, P.; Wu, L.; Dou, H.; Zhang, X., 2D MXene/SnS_2 composites as high-performance anodes for sodium ion batteries. *Chemical Engineering Journal* **2018,** 334, 932-938.

35. Hui, X.; Zhao, R.; Zhang, P.; Li, C.; Wang, C.; Yin, L., Low‐Temperature Reduction Strategy Synthesized Si/Ti_3C_2 MXene Composite Anodes for High‐Performance Li‐Ion Batteries. *Advanced Energy Materials* **2019,** 9, (33).

36. Xie, X.; Zhao, M.-Q.; Anasori, B.; Maleski, K.; Ren, C. E.; Li, J.; Byles, B. W.; Pomerantseva, E.; Wang, G.; Gogotsi, Y., Porous heterostructured MXene/carbon nanotube composite paper with high volumetric capacity for sodium-based energy storage devices. *Nano Energy* **2016,** 26, 513-523.

37. Zhao, M. Q.; Ren, C. E.; Ling, Z.; Lukatskaya, M. R.; Zhang, C.; Van Aken, K. L.; Barsoum, M. W.; Gogotsi, Y., Flexible MXene/carbon nanotube composite paper with high volumetric capacitance. *Adv Mater* **2015,** 27, (2), 339-45.

38. Yan, J.; Ren, C. E.; Maleski, K.; Hatter, C. B.; Anasori, B.; Urbankowski, P.; Sarycheva, A.; Gogotsi, Y., Flexible MXene/Graphene Films for Ultrafast Supercapacitors with Outstanding Volumetric Capacitance. *Advanced Functional Materials* **2017,** 27, (30).

39. Guo, X.; Zhang, J.; Song, J.; Wu, W.; Liu, H.; Wang, G., MXene encapsulated titanium oxide nanospheres for ultra-stable and fast sodium storage. *Energy Storage*

Materials **2018,** 14, 306-313.

40. Zhao, M. Q.; Xie, X.; Ren, C. E.; Makaryan, T.; Anasori, B.; Wang, G.; Gogotsi, Y., Hollow MXene Spheres and 3D Macroporous MXene Frameworks for Na-Ion Storage. *Adv Mater* **2017,** 29, (37).

41. Liu, Y. T.; Zhang, P.; Sun, N.; Anasori, B.; Zhu, Q. Z.; Liu, H.; Gogotsi, Y.; Xu, B., Self-Assembly of Transition Metal Oxide Nanostructures on MXene Nanosheets for Fast and Stable Lithium Storage. *Adv Mater* **2018,** 30, (23), e1707334.

42. Sang, X.; Xie, Y.; Lin, M. W.; Alhabeb, M.; Van Aken, K. L.; Gogotsi, Y.; Kent, P. R. C.; Xiao, K.; Unocic, R. R., Atomic Defects in Monolayer Titanium Carbide ($Ti_3C_2T_x$) MXene. *ACS Nano* **2016,** 10, (10), 9193-9200.

43. Dillon, A. D.; Ghidiu, M. J.; Krick, A. L.; Griggs, J.; May, S. J.; Gogotsi, Y.; Barsoum, M. W.; Fafarman, A. T., Highly Conductive Optical Quality Solution-Processed Films of 2D Titanium Carbide. *Advanced Functional Materials* **2016,** 26, (23), 4162-4168.

44. Blöchl, P. E., Projector augmented-wave method. *Phys. Rev. B* **1994,** 50, (24), 17953-17979.

45. Kresse, G.; Furthmuller, J., Efficient iterative schemes for ab initio total-energy calculations using a plane-wave basis set. *Phys. Rev. B* **1996,** 54, (16), 11169-11186.

46. Kresse, G.; Hafner, J., Ab initiomolecular dynamics for liquid metals. *Phys. Rev. B* **1993,** 47, (1), 558-561.

47. Perdew, J. P.; Burke, K.; Ernzerhof, M., Generalized gradient approximation made simple. *Phys. Rev. Lett.* **1996,** 77, (18), 3865-3868.

48. Ma, X.; Zou, L.; Zhao, W., Tailoring hollow microflower-shaped $CoSe_2$ anodes in sodium ion batteries with high cycling stability. *Chem Commun (Camb)* **2018,** 54, (74), 10507-10510.

49. Park, S. K.; Kang, Y. C., MOF-Templated N-Doped Carbon-Coated $CoSe_2$

Nanorods Supported on Porous CNT Microspheres with Excellent Sodium-Ion Storage and Electrocatalytic Properties. *ACS Appl Mater Interfaces* **2018,** 10, (20), 17203-17213.

50. Wu, X.; Wang, Z.; Yu, M.; Xiu, L.; Qiu, J., Stabilizing the MXenes by Carbon Nanoplating for Developing Hierarchical Nanohybrids with Efficient Lithium Storage and Hydrogen Evolution Capability. *Adv Mater* **2017,** 29, (24).

51. Wang, Y.; Li, Y.; Qiu, Z.; Wu, X.; Zhou, P.; Zhou, T.; Zhao, J.; Miao, Z.; Zhou, J.; Zhuo, S., Fe_3O_4@Ti_3C_2 MXene hybrids with ultrahigh volumetric capacity as an anode material for lithium-ion batteries. *Journal of Materials Chemistry A* **2018,** 6, (24), 11189-11197.

52. Meng, R.; Huang, J.; Feng, Y.; Zu, L.; Peng, C.; Zheng, L.; Zheng, L.; Chen, Z.; Liu, G.; Chen, B.; Mi, Y.; Yang, J., Black Phosphorus Quantum Dot/Ti_3C_2 MXene Nanosheet Composites for Efficient Electrochemical Lithium/Sodium-Ion Storage. *Advanced Energy Materials* **2018,** 8, (26).

53. Huang, H.; Cui, J.; Liu, G.; Bi, R.; Zhang, L., Carbon-Coated $MoSe_2$/MXene Hybrid Nanosheets for Superior Potassium Storage. *ACS Nano* **2019,** 13, (3), 3448-3456.

54. Li, Z.; Xue, H.; Wang, J.; Tang, Y.; Lee, C.-S.; Yang, S., Reduced Graphene Oxide/Marcasite-Type Cobalt Selenide Nanocrystals as an Anode for Lithium-Ion Batteries with Excellent Cyclic Performance. *ChemElectroChem* **2015,** 2, (11), 1682-1686.

55. Li, B.; Wang, R.; Chen, Z.; Sun, D.; Fang, F.; Wu, R., Embedding heterostructured MnS/$Co_{1-x}S$ nanoparticles in porous carbon/graphene for superior lithium storage. *Journal of Materials Chemistry A* **2019,** 7, (3), 1260-1266.

56. Teng, Y.; Zhao, H.; Zhang, Z.; Li, Z.; Xia, Q.; Zhang, Y.; Zhao, L.; Du, X.; Du, Z.; Lv, P.; Swierczek, K., MoS_2 Nanosheets Vertically Grown on Graphene Sheets for

Lithium-Ion Battery Anodes. *ACS Nano* **2016,** 10, (9), 8526-35.

57. Zheng, Z.; Zao, Y.; Zhang, Q.; Cheng, Y.; Chen, H.; Zhang, K.; Wang, M.-S.; Peng, D.-L., Robust erythrocyte-like Fe_2O_3@carbon with yolk-shell structures as high-performance anode for lithium ion batteries. *Chemical Engineering Journal* **2018,** 347, 563-573.

58. Dou, Y.; Xu, J.; Ruan, B.; Liu, Q.; Pan, Y.; Sun, Z.; Dou, S. X., Atomic Layer-by-Layer Co_3O_4/Graphene Composite for High Performance Lithium-Ion Batteries. *Advanced Energy Materials* **2016,** 6, (8).

59. Qin, J.; Wang, T.; Liu, D.; Liu, E.; Zhao, N.; Shi, C.; He, F.; Ma, L.; He, C., A Top-Down Strategy toward SnSb In-Plane Nanoconfined 3D N-Doped Porous Graphene Composite Microspheres for High Performance Na-Ion Battery Anode. *Adv Mater* **2018,** 30, (9).